Journal of Materials Chemistry C

PAPER

View Article Online
View Journal | View Issue

Cite this: J. Mater. Chem. C, 2019, 7, 3003

Lead-free hybrid ferroelectric material based on formamidine: $[NH_2CHNH_2]_3Bi_2I_9$†

Przemysław Szklarz, *[a] Anna Gągor, [b] Ryszard Jakubas, [a] Piotr Zieliński, [c] Anna Piecha-Bisiorek, [a] Jakub Cichos, [a] Mirosław Karbowiak, [a] Grażyna Bator *[a] and Agnieszka Ciżman [d]

The extraordinary thermal stability of $[NH_2CHNH_2]_3Bi_2I_9$ ($FA_3Bi_2I_9$) crystals, up to around 600 K, has been enhanced by using the evaporating method. DSC measurements have revealed reversible structural phase transitions: at 203 K (Phase I → Phase II), 173 K (II → III), 134.7 K (III → IV), 131.4 K (IV → V), and 120 K (V → VI). The crystal structures of $FA_3Bi_2I_9$ adopt the polar space groups $P6_3mc$ at 220 K (Phase I) and $Cmc2_1$ at 190 K (Phase II). The pyroelectric current (I_{pyr}) measured in the temperature range covering all the phases of $FA_3Bi_2I_9$ confirmed their polar nature. The reversibility of the spontaneous polarization in each phase has been confirmed by the observed hysteresis loops. All the phase transitions are dielectrically active. The dielectric response ($\varepsilon^*(\omega,T)$ close to 134.7 and 131.4 K) is characteristic of ferroelectrics with a critical slowing-down process. Optical bandgaps estimated from the UV-vis measurements and calculated using the DFT method are equal to 1.85 and 1.89 eV, respectively. On the basis of the structural, dielectric, and spectroscopic results, the molecular mechanisms of the phase transitions have been proposed.

Received 21st December 2018,
Accepted 4th February 2019

DOI: 10.1039/c8tc06458j

rsc.li/materials-c

Introduction

Novel materials suitable for use in high-efficiency photovoltaic cells have garnered the interest of many leading laboratories. The desired material should fulfill many requirements, namely, an appropriate bandgap and current carrier concentration. Moreover, it should be stable in the ambient atmosphere without any obvious degradation over thousands of hours of use under standard illumination and humidity conditions. Further, it is desirable that the electron acceptor and donor energy levels are compatible with standard n and p organic semiconductors, commercially available and usually applied in solar cells.

Several methods are, therefore, necessary to estimate the usefulness of such materials for application in photovoltaic devices. The measurements of electric conductivity as well as ultraviolet-visible (UV-vis) and photoluminescence are required. Understanding the crystal structure and electronic density of states in the band structure are crucial in the determination of possible direct or indirect electron transitions and other semiconductor properties of the material.

Molecular ionic crystals designed to exhibit order–disorder phenomena have gained immense interest both from the technological and fundamental standpoints. The effect of different organic molecules, incorporated into the crystal structure, on the underlying structure and phase transitions (PTs) is well known for the $FABX_3$-type family (where FA = $CH(NH_2)_2$; B = Pb or Sn; X = I).[1–4] These materials exhibit promising efficiency toward the conversion of solar light into electrical energy, although their stability is considerably insufficient for practical use.

In the search for novel materials, which may face competition from organic–inorganic hybrid perovskites based on lead, we focus our attention on halobismuthate(III) and haloantimonate(III) compounds. They are described by the general formula $R_aM_bX_{3b+a}$, (where R denotes organic cations; M stands for Sb(III) or Bi(III); and X = Cl, Br, or I). They exhibit a rich diversity of anionic structures (from zero- to one-, two-, or even three-dimensional (0D, 1D, 2D, or 3D, respectively) architectures) and isoelectronicity with Sn(II) and Pb(II).[5–9] Their ferroelectric properties were found in four subclasses, *i.e.*, RMX_4, $R_3M_2X_9$, R_2MX_5, and $R_5M_2X_{11}$.[10–15] Recently, several reports have focused on compounds with the $R_3M_2X_9$ stoichiometry, which can crystallize

[a] Faculty of Chemistry, University of Wrocław, F. Joliot-Curie 14, 50-383 Wrocław, Poland. E-mail: przemyslaw.szklarz@chem.uni.wroc.pl, grazyna.bator@chem.uni.wroc.pl
[b] W. Trzebiatowski Institute of Low Temperature and Structure Research Polish Academy of Science, P.O. Box 1410, 50-950 Wrocław, Poland
[c] The H Niewodniczański Institute of Nuclear Physics Polish Academy of Science, Radzikowskiego 152, PL-31-342 Kraków, Poland
[d] Department of Experimental Physics, Faculty of Fundamental Problems of Technology, Wrocław University of Science and Technology, Wybrzeże Wyspiańskiego 27, 50-370 Wrocław, Poland

† Electronic supplementary information (ESI) available. CCDC 1855907 and 1855908. For ESI and crystallographic data in CIF or other electronic format see DOI: 10.1039/c8tc06458j

either as infinite 1D double chains,[16] 2D layers,[6] discrete bi-octahedral (0D),[17] or four-octahedral (0D) units $[M_4X_{18}]$.[18] It has been revealed that ferroelectric properties were found to appear only in the derivatives characterized by 0D or 2D anionic layers. The most attractive materials, from the viewpoint of optoelectronic applications as light absorbers for photovoltaic cells, appear to be iodide analogs—$R_3Bi_2I_9$ (where R refers to small-size organic cations or monovalent metallic ones, namely, Cs, Rb, or Ag). It is noteworthy that all the known iodide ferroelectric analogues adopt only the 0D anionic structure.

Organic–inorganic hybrids based on formamidinium (FA) cations, which exhibit ferroelectric properties, are unique. Until now, only two examples of ferroelectrics are known among compounds within the perovskite family, namely, $FASnI_3$[3] and $FAPbI_3$.[19] Therefore, we decided to place the polar FA cation into the iodobismuthate network and to determine the physicochemical properties of such materials. In practice, it is often observed that materials, which exhibit ferroelectricity at lower temperatures, exhibit semiconductor properties at higher temperatures.[20]

In this work, we report a novel Bi-based ferroelectric material of $(NH_2CHNH_2)_3Bi_2I_9$ ($FA_3Bi_2I_9$), which reveals polar properties in numerous (six) successive phases. We present detailed investigations of its crystal structures, dielectric and electronic properties, and analyze its intriguing ferroelastic domain structure. $FA_3Bi_2I_9$ is a material characterized by a 0D (isolated bi-octahedra) anionic network. A rich polymorphism of $FA_3Bi_2I_9$ in the solid state has been confirmed by thermal methods (differential scanning calorimetry (DSC) and dilatometry) and optical observations. Spontaneous polarization reversibility has been confirmed by both observation of ferroelectric hysteresis and pyroelectric measurements. The physicochemical properties of $FA_3Bi_2I_9$ are compared with those observed for other halobismuthate(III) and haloantimonate(III) compounds among the $R_3M_2X_9$-type ferroelectrics.

Experimental

Synthesis

All the materials needed for the synthesis of $[NH_2CHNH_2]_3Bi_2I_9$ ($FA_3Bi_2I_9$) were purchased from commercial sources (Sigma-Aldrich and Merck (HI)) and used without further purification: $[NH_2CHNH_2]\cdot I$ (>98%), BiI_3 (>99.998%), and HI (57%). The crystals were grown by the slow evaporation of a concentrated HI solution containing 3 : 2 ratio of $[NH_2CHNH_2]\cdot I$ and BiI_3. The salts obtained were recrystallized twice from a methanol solution, and their compositions were verified by elemental analysis: C: 2.15% (theor. 2.13%), N: 4.98% (theor. 4.96%), and H: 1.05% (theor. 1.01%). The single crystals were grown from an aqueous solution at room temperature (RT).

Thermal analysis

DSC experiments were carried out using a PerkinElmer DSC 8500 differential scanning calorimeter at a scanning rate of 4 K min^{-1} in the temperature range of 100–300 K. In the DSC measurements under a nitrogen atmosphere, the polycrystalline material was placed in hermetically sealed Al pans. Calibration was performed with *n*-heptane and indium as the standard. Dilatometric measurements (TMA) were performed with the thermomechanical analyzer PerkinElmer TMA 7 in the temperature range of 150–300 K at a temperature rate of 4 K min^{-1}. Liquid nitrogen was used as the cooling medium. Simultaneous thermogravimetric analysis (TGA) and differential thermal analysis (DTA) were performed using a Setaram SETSYS 16/18 instrument in the temperature range of 300–780 K at a ramp rate of 5 K min^{-1}. The scans were performed under flowing nitrogen (flow rate: 1 dm^3 h^{-1}).

Single-crystal X-ray diffraction (XRD)

For all the structures: $C_3H_{15}Bi_2I_9N_6$, M_r = 1695.27 experiments were carried out with MoKα radiation using an Xcalibur, Atlas instrument. Absorption was corrected by multi-scan methods, CrysAlis(PRO) 1.171.38.43 (Rigaku Oxford Diffraction, 2015). Empirical absorption was amended using spherical harmonics, implemented in SCALE3 ABSPACK scaling algorithm. SHELXL2014/7 software was used for structure solution and refinement. The positions of hydrogen atoms were determined from the geometry and refined as riding atoms. Their positions should be considered only as a structure decoration because of a disorder.

Dielectric and polar properties' measurements

The complex dielectric permittivity, $\varepsilon^* = \varepsilon' - i\varepsilon''$, was measured using a single-crystal $FA_3Bi_2I_9$ with the use of an Agilent E4980A Precision LCR Meter operated between 90 and 300 K in the frequency range between 135 Hz and 2 MHz. The overall errors were less than 5%. The dimensions of the crystal were 5 × 3 × 0.75 mm^3. The pyroelectric properties were determined by using an electrometer/high-resistance meter Keithley 6517B with a temperature ramp of 2 K min^{-1} in the same temperature range. Ferroelectric hysteresis loops were determined using a modified Sawyer–Tower circuit at 50 Hz.

Optical measurements

The ferroelastic domain structures of several $FA_3Bi_2I_9$ crystals were studied by means of an Olympus BX53 optical polarization microscope. The samples were placed in the LINKAM THMS600 heating/cooling stage, where the temperature was stabilized to within 0.1 K.

UV-vis spectra

The absorption spectra in the wavelength range of 300–600 nm were recorded on a Cary 5000 UV/vis/NIR instrument. The spectra of the powder in Nujol were measured at RT. Then, the spectra were corrected by subtracting the background of Nujol. The band structure and projected density of states (PDOS) were calculated using WIEN2k software[21] (PBE functional[22]). K-path for the band structure calculation was prepared using XCrysDen[23] software.

Results

Thermal properties (TGA, DTA, DSC, and TMA)

The thermal stability of the $FA_3Bi_2I_9$ sample was determined by performing simultaneous TGA and DTA between 300 and 780 K. The resulting traces are shown in Fig. S1 (ESI†). $FA_3Bi_2I_9$ exhibits an endothermic effect at *ca.* 600 K in the DTA traces. The crystal seems to be stable up to about 600 K. Above this temperature, the loss of weight starts to exceed 1.5%, which is characteristic of the onset of compound decomposition.

DSC revealed a very complex PT sequence for $FA_3Bi_2I_9$. The DSC traces for $FA_3Bi_2I_9$ are shown in Fig. 1. In the low-temperature region (between 300 and 110 K), four reversible heat anomalies assigned to structural PTs are evident: at 203/203 (Phase I ↔ Phase II), 174.6/176.9 (II ↔ III), 131.3/131.3 (III ↔ IV), and 117/120 K (V ↔ VI) on heating–cooling.

Taking into account the shapes of thermal anomalies and temperature hystereses, PTs can be classified as follows: I ↔ II continuous (second order), II ↔ III close to second order, III ↔ IV discontinuous, and VI ↔ V clearly discontinuous (first order). Entropy changes (ΔS) estimated for these transitions are as follows: $\Delta S_{(II \leftrightarrow III)}$ = 1.3, $\Delta S_{(III \leftrightarrow IV)}$ = 2.72, and $\Delta S_{(IV \leftrightarrow V)}$ = 13.2 J mol^{-1} K^{-1}. The values of the transition entropy for the two lowest-temperature PTs are characteristic of the transitions with an order–disorder mechanism, whereas for the two remaining PTs, we can postulate a displacive mechanism.

Fig. S2 (ESI†) shows the results of the linear thermal expansion ($\Delta L/L_0$) measurements along the *c*-axis (Phase I, $P6_3mc$). We show the runs registered during cooling and heating of the sample. It should be emphasized that the dilation anomalies were perfectly reversible. Four thermal anomalies were detected: at 200 K and 175 K, they manifested themselves as changes in the slopes of dilation (continuous transitions), whereas at 133 and 113 K, a rapid expansion of the sample took place that is characteristic of discontinuous transitions. The sequence of PTs detected by dilatometric measurements is in full agreement with those observed in calorimetric studies.

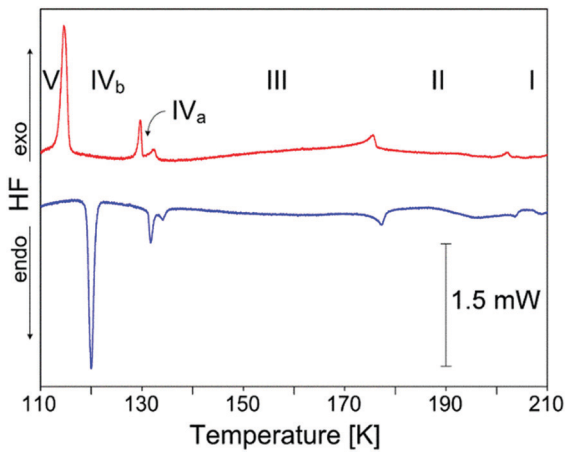

Fig. 1 DSC curves of $FA_3Bi_2I_9$ crystal measured upon the heating and cooling of a sample.

Crystal structure of $FA_3Bi_2I_9$

The thermal evolution of the lattice parameters reveals five polymorphs of $FA_3Bi_2I_9$ at low temperatures (Fig. 2).

The first one, Phase I, is hexagonal with the unit cell parameters a = 8.71(1) Å, c = 22.01(1) Å, and γ = 120°. The hexagonal system is commonly observed in analogous compounds. Literature survey shows that $MA_3Bi_2I_9$ (MA: methylammonium)[24] as well as guanidinium-based[25] and imidazolium-based[26] hybrids crystallize in the centrosymmetric space group $P6_3/mmc$. All of them are isotypic to the inorganic $Cs_3Bi_2I_9$,[27] the structure of which is virtually identical to $Cs_3Cr_2Cl_9$.[28] In addition, a majority of $A_3M_2X_9$ compounds (where A stands for a metal ion), which are characterized by $M_2X_9^{3-}$ ions, adopt the centrosymmetric $P6_3/mmc$ or $P6_3/m$ space groups.[29] Accordingly, the crystal structure of Phase I was resolved in the first approximation in the centrosymmetric space group. However, the results of the dielectric measurements, particularly the presence of a spontaneous polarization hysteresis loop, unequivocally indicate the lack of a symmetry center. Hence, the final model of the structure of Phase I was resolved in the noncentrosymmetric, polar space group $P6_3mc$ (no. 186).

The PT at T_{c1} is associated with the lowering of the crystal class to orthorhombic $Cmc2_1$ (No. 36) and pseudo-merohedral

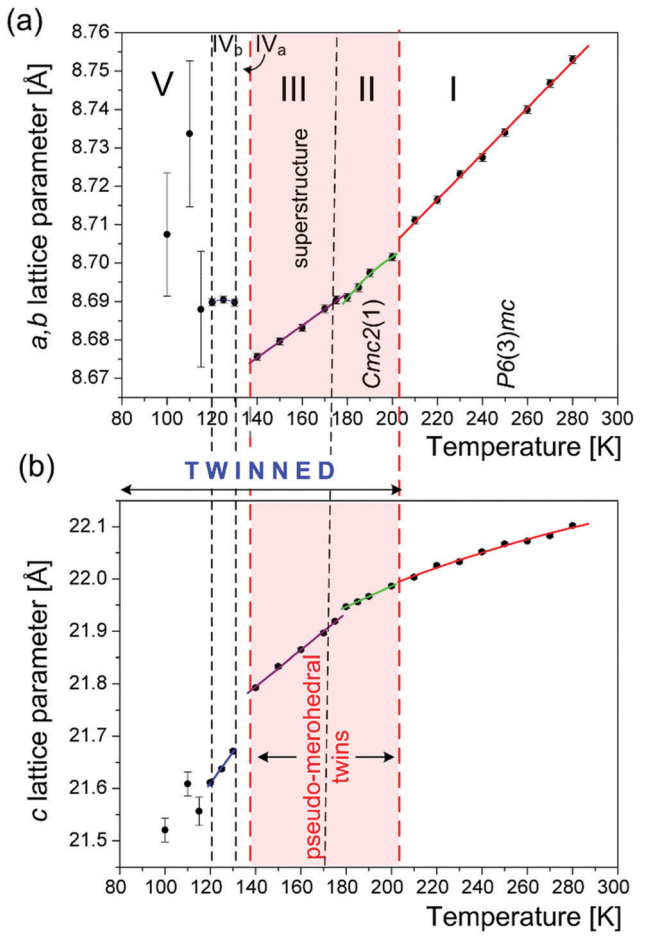

Fig. 2 Thermal evolution of hexagonal lattice parameters. Temperatures of the PTs, T_{ci}, obtained from the DSC are marked. Lines serve as guidelines.

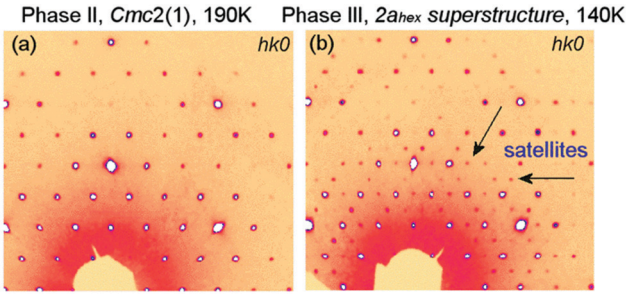

Fig. 3 Reciprocal space reconstructions of *hk*0 layers in Phase II (190 K) and Phase III (140 K). The additional peaks from the superstructure are present in Phase III.

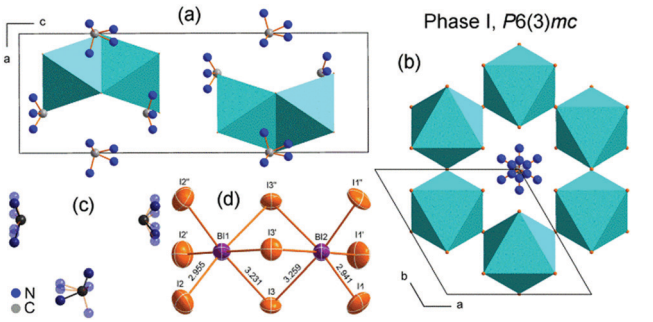

Fig. 4 Crystal structure of $FA_3Bi_2I_9$ in Phase I, T = 220 K; (a) the structure comprises isolated $Bi_2I_9^{3-}$ bi-octahedra and disordered FA^+ cations; (b) view along the hexagonal *c*-axis; (c) three symmetry-inequivalent FA^+ disordered along the 3-fold axis; (d) basic unit of the inorganic substructure in ellipsoid representation at 50% probability.

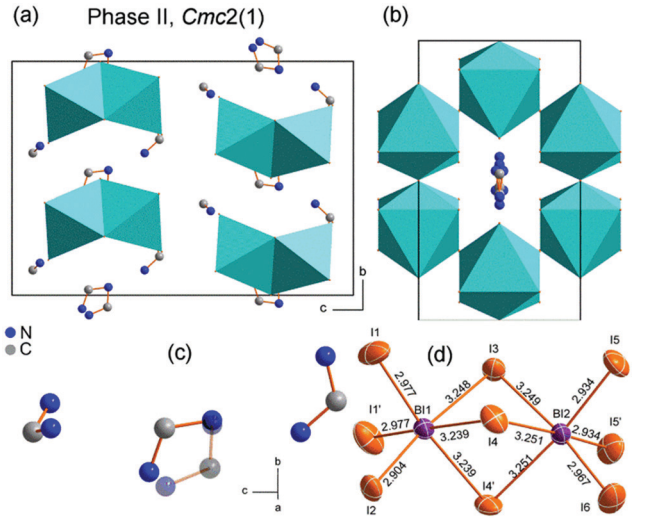

Fig. 5 Crystal structure of $FA_3Bi_2I_9$ in Phase II, T = 190 K; (a) $Bi_2I_9^{3-}$ bi-octahedra are tilted from the *b*-axis; (b) view along the hexagonal *c*-axis; (c) symmetry-inequivalent FA^+ cations; (d) basic unit of the inorganic substructure in ellipsoid representation at 50% probability.

twinning. Both phases are group–subgroup related. The $Cmc2_1$ space group is the maximal non-isomorphic subgroup of $P6_3mc$ with index 3, which defines the number of orientation states for the twin domains.[30] The PT belongs to the Aizu species, namely, $6mmF2mm$.[31] It is interesting that the ratio of the lattice parameters b/a is very close to $\sqrt{3}$, *i.e.*, to that of the hexagonal structure. Therefore, the lattices of the domain states coincide and the diffraction pattern corresponds to a pseudohexagonal lattice. This is shown in Fig. 3a, which reveals the reciprocal space reconstruction of the *hk*0 layer in Phase II, at T = 190 K. Fig. 3b shows the same *hk*0 layer in Phase III, at 140 K. After the second PT at T_{c2} additional, weak peaks appear, which may be indexed in a doubled 2a or 2b orthorhombic (or $2a_{hex}$) superstructure. Similar to Phase II, the lattices of the twin domains coincide, yielding a pseudohexagonal lattice. The average structure (based only on the main peaks excluding the weak satellites) can be refined with $Cmc2_1$ symmetry ($R_1 \sim 0.06$) and has similar atomic arrangement as that of Phase II. Because of the combination of twinning and the very weak intensities of the satellite peaks, we decided not to speculate on the possible structural model of this phase.

Further cooling induces structural deformations that result in a heavily twinned diffraction picture with partially coinciding twin lattices and split diffraction peaks with remarkably reduced intensities. Due to the complex twinning present in $FA_3Bi_2I_9$, their crystal structures have been resolved only in Phases I and II. The results are presented below.

Phase I. The inorganic part in Phase I comprises isolated $Bi_2I_9^{3-}$ bi-octahedra. The asymmetric unit contains two Bi^{3+} and three I^- ions. The Bi^{3+} cation occupies the C_{3v} symmetry site; the I^- ions are located on the C_s position and are populated by a 3-fold axis. The negative charge is balanced by three FA^+ ions, which are heavily disordered in Phase I. Each cation adopts at least three different positions. Fig. 4 shows the packing and details of the crystal structure of $FA_3Bi_2I_9$ in Phase I.

Phase II. The PT at T_{c1} affects both the inorganic part and counterions. The details of the structure at 190 K are shown in Fig. 5. Symmetry reduction to orthorhombic $Cmc2_1$ induces distortion in $Bi_2I_9^{3-}$ bi-octahedra, which lose the 3-fold symmetry and tilt from the *b*-direction (Fig. 5(a) and (b)). At the same time, the FA^+ cations become partially ordered (Fig. 5(c)). As far as the anions are concerned, the number of I^- ligands in the asymmetric unit is doubled to six as compared to that in the high-temperature phase. The $Bi_2I_9^{3-}$ bi-octahedra possess C_s symmetry with the mirror plane passing through both Bi^{3+} and three iodine positions (I(2), I(3), and I(6)), as shown in Fig. 5(d). It appears that the pronounced disorder of FA^+ is reduced in Phase II, partially due to the loss of the 3-fold axis along the *c*-direction. In Phase II, the cations may adopt the C_1 or C_s symmetry. Due to the twinning of the sample, the exact location of all the possible orientation states of ions may not be extracted from the diffraction data; therefore, the presented model should be considered as qualitative rather than quantitative.

In Phases I and II, N–H···I and C–H···I contacts, which meet the criteria for the presence of hydrogen bonds (HBs),[32] are abundant. However, in the absence of an unambiguous set of FA^+ positions, due to the dynamic and/or static disorder of cations, it is difficult to determine the actual geometry of these interactions. One of the questions that arise is whether these HBs have any impact on the structure of the high-temperature

phases or not. In the following, we show that because of the dynamic characteristic of the FA^+ disorder, HBs primarily provide specificity rather than stability for the consecutive phases; this occurs, at least, at temperatures at which the cation motion is frozen.

By analyzing the possible positions of the cations, it is evident that the distinct reorientations that occur during the first phase transformation (associated with the loss of the 3-fold axis) affect the inorganic part of the structure, as shown in Fig. 4c and 5c.

In Phase I, all the iodide ions may act as multiple acceptors for numerous forked HBs (see Fig. 6a). In Phase II, the surroundings of the iodide ions and availability of possible hydrogen donors dramatically change. The distribution of positive charges around the bi-octahedra becomes much more asymmetrical, which is shown in Fig. 6b.

Accordingly, $Bi_2I_9^{3-}$ octahedrons become more distorted. The most identifiable changes occur in the positions of the terminal iodides, which may shift even by 0.28(1)–0.30(1) Å from the initial placements. Despite the steric effects, which may influence the position and shape of the bi-octahedra, the remarkable change in the specific Bi–I distances is also evident. The apical I(2) iodide atoms stop acting as acceptors in the HBs as a result of these cation reorientations. Consequently, the Bi(1)–I(2) distance is remarkably shortened (from 2.955(1) to 2.904(1) Å). It is worth noting that such a significant contraction of the Bi–I distance concerns only the I(2) iodide atoms; the remaining ones, which still interact in HBs, experience marginal changes. With decreasing temperatures, some of these distances even increase, which may imply strengthening of the HB interactions (Bi(1)–I(1) changes from 2.955(1) at 220 K to 2.975(1) Å at 190 K). In addition, the anisotropic displacement parameters (ADPs) of I(2) are reduced (compared to other ADPs of iodide ligands). The ADPs may be indicators of the degree of disorder around the iodine acceptors. These iodine atoms, which act as multiple acceptors, are spatially frustrated and their ADPs are larger.

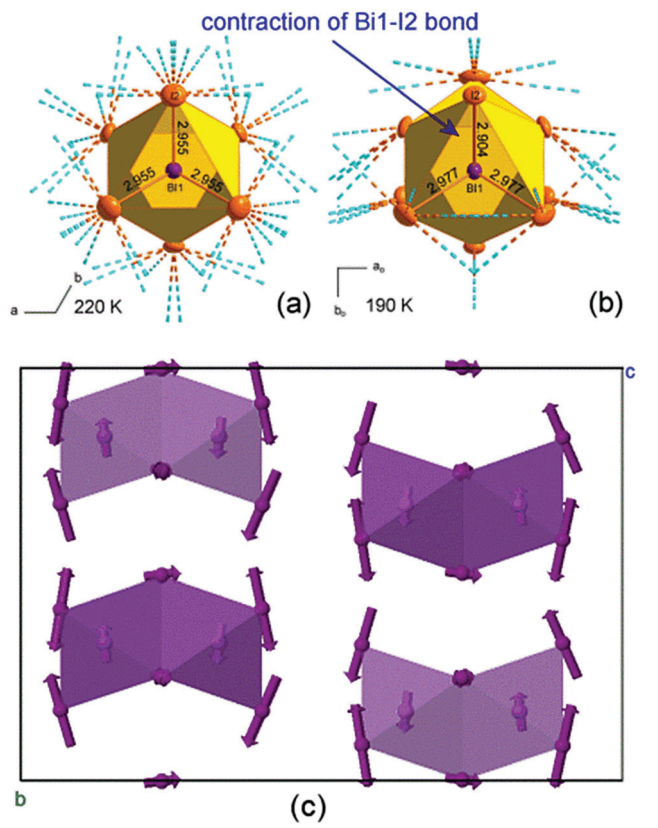

Fig. 6 Distribution of possible N–H···I and C–H···I contacts around the $[Bi_2I_9]^{3-}$ bi-octahedra in (a) Phase I and (b) Phase II, and the maximum H···I distance is equal to 3.3 Å (boundary of the Jeffrey's criteria); (c) distortion modes for $[Bi_2I_9]^{3-}$ due to the octahedral distortion in Phase II ($Cmc2_1$).

Despite these HB interactions, octahedral distortion may be induced by the changes in the activity of the Bi^{3+} lone-electron pair. In both Phases I and II, Bi^{3+} is displaced from the geometric center of the iodide ligands, which indicates the aspherical distribution of $6s^2$ electrons and their interactions with the electronic p states of I^-. The change in the lone-pair activity of Bi^{3+} has been recognized as a source of the structural PT in 2-MImSbI$_4$ and 2-MImBiI$_4$ hybrids with extended 1D anions;[33,34] it is also considered as an important source of polar displacements or locally distorted states in hybrid perovskites bearing Pb^{2+} or Sn^{2+} ions.[35,36] The octahedral distortion parameters Δ_d and angle variance σ^2 [37] for Bi(1)I$_6$ grow in Phase II, yielding increased distortion: Δ_d increases from $1.99(1) \times 10^{-3}$ to $2.24(1) \times 10^{-3}$, whereas σ^2 changes from 14.88(6) to 16.45(5). However, in the case of the second octahedron Bi(2)I$_6$, both Δ_d and σ^2 are lower in Phase II (Δ_d decreases from $2.63(1) \times 10^{-3}$ to $2.44(1) \times 10^{-3}$; σ^2 is reduced from 20.95(5) to 17.92(5)). Fig. 5 shows the displacements of Bi^{3+} and I^- atoms from the high-temperature sites responsible for octahedral distortion. The lengths of the arrows in Fig. 6 represent the amplitude of the displacements, which are the smallest for the bridging iodide atoms (0.09–0.17 Å), and the largest for the apical iodine atoms ($\sim$0.29(1) Å). The Bi displacements are equal to $\sim$0.14 Å. The total distortion amplitude for the inorganic part of the asymmetric unit is equal to 1.10(1) Å (AMPLIMODES[38]). The detailed bond lengths are shown in Fig. 4 and 5.

In the light of the above, it seems that the polar properties of $FA_3Bi_2I_9$ can be attributed to the orientational ordering of the FA^+ dipoles, as well as the polar distortions of the complex anions.

Dielectric measurements

Dielectric spectroscopy was used to characterize the dynamics of the dipolar cations and their contribution to the molecular mechanism of successive PTs below RT. Fig. 7 shows the results of the measurements of the complex electric permittivity ($\varepsilon^* = \varepsilon' - i\varepsilon''$) in the kilohertz-frequency region.

It is evident that the dielectric response ($\varepsilon'(T,\omega)$) clearly reflects the presence of structural PTs, which is in agreement with those revealed by the calorimetric studies. The I $\rightarrow$ II and II $\rightarrow$ III PTs are accompanied by fairly weak dielectric anomalies (see Fig. 7a). The III $\rightarrow$ IV PT exhibits a very complex response

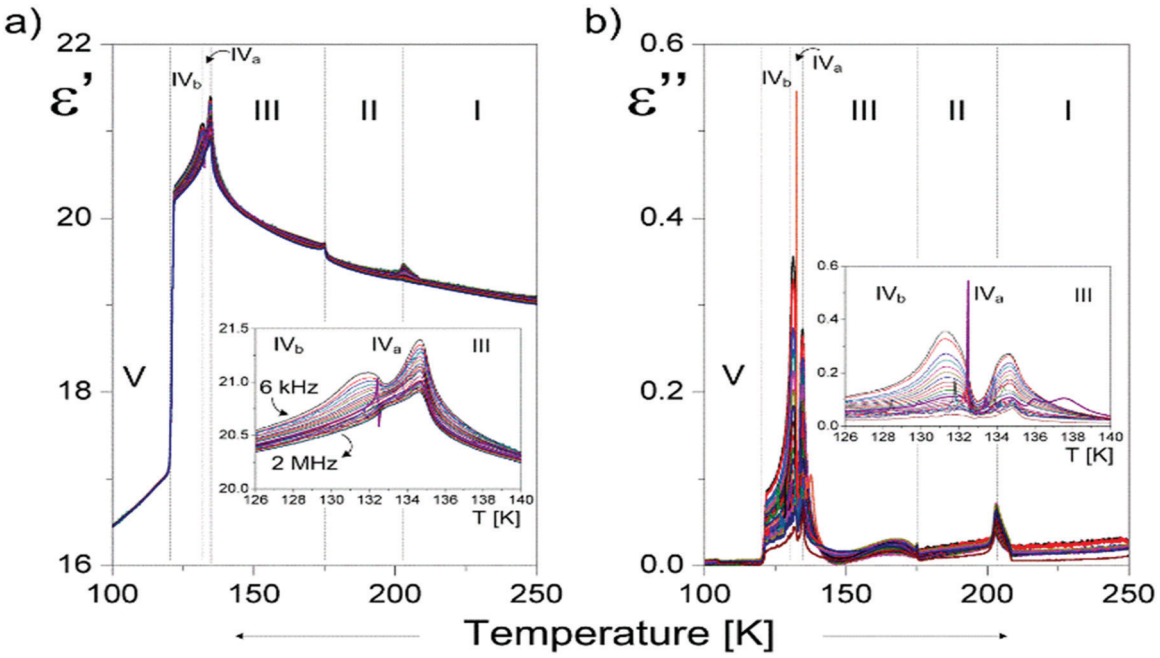

Fig. 7 Temperature dependence of (a) real and (b) imaginary parts of the complex electric permittivity of $FA_3Bi_2I_9$.

since the emerging anomaly exhibits a double peak. Approaching 135 K, ε' critically increases up to $\varepsilon_{max}' \approx 22$ and then a practically similar peak appears at four degrees below. The dielectric anomaly in this temperature region is puzzling. It is difficult to state if we encounter an intermediate phase between 135 and 131 K or that the III → IV PT experiences two steps. The lowest-temperature PT at 120 K is accompanied by an abrupt decrease in ε' down to 16 units, which indicates drastic freezing of the dipolar cation motion. The imaginary part of permittivity (ε'') *versus* temperature, as shown in Fig. 7b, shows only marginal changes around the I → II, II → III, and IV → V PTs, and no dielectric relaxation processes are visible in a wide temperature region, except for Phase IV. Both peaks of ε' are accompanied by a distinct anomaly of ε''. The dielectric response around the III → IV PT exhibits the feature characteristic of the critical slowing down of the macroscopic relaxation time encountered in the "order–disorder" ferroelectrics. At 155 kHz, in Phase IV, the evident piezoelectric properties of $FA_3Bi_2I_9$ are revealed.

The ac conductivity, σ_{ac}, of $FA_3Bi_2I_9$ was measured above RT (Fig. 8). The obtained results are discussed in terms of the Jonscher universal power law:[39]

$$\sigma_{ac}'(T,\omega) = \sigma_{dc}(T) + \varepsilon_0\omega\varepsilon''(T,\omega) = \sigma_{dc}(T) + A\omega^s \qquad (1)$$

where $A\omega^s$ describes the frequency-dependent ac conductivities, where A is a constant dependent on temperature; s is a power exponent, which is generally less than or equal to 1; $\omega = 2\pi f$ (f (Hz)) is the angular frequency; and ε_0 is the vacuum permittivity. For the obtained results, the ac conductivity spectra at different temperatures were fitted to eqn (1), and the parameters σ_{dc}, A, and s were extracted from this analysis. The results of the adjustment are presented as continuous lines in Fig. 8.

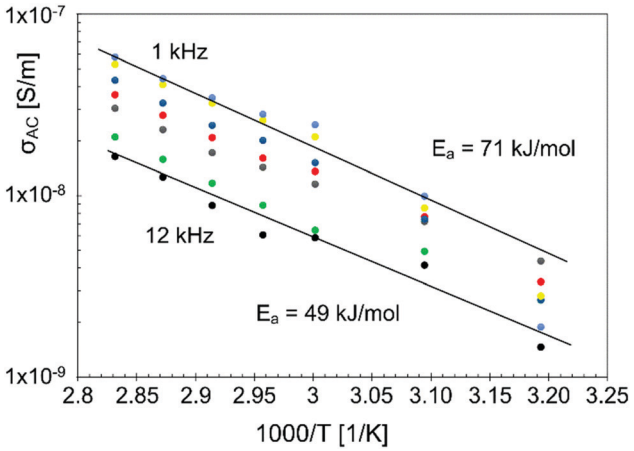

Fig. 8 ac conductivity (log scale) *versus* reciprocal temperature, 1000/T, of $FA_3Bi_2I_9$.

The frequency dependence of ac conductivity and temperature dependence of the s parameter (see Fig. S3, ESI†) are characteristic of the activation process of the electrical carriers. The reciprocal temperature dependence of σ_{ac} for $FA_3Bi_2I_9$ is shown in Fig. 8 as an Arrhenius plot representation, namely, $\ln(\sigma_{ac})$ *vs.* 1000/T. The value of the estimated bandgap for the conductivity at 1 kHz equals to 0.736 eV.

Pyroelectric measurements

The measurements of the pyroelectric current (I_{pyr}) carried out in the temperature range covering all the phases of $FA_3Bi_2I_9$ revealed a very complex picture. The measurements were performed in two ways. The first experiment ($I_{pyr}(T)$) was done without any pooling of the sample, which was cooled down to

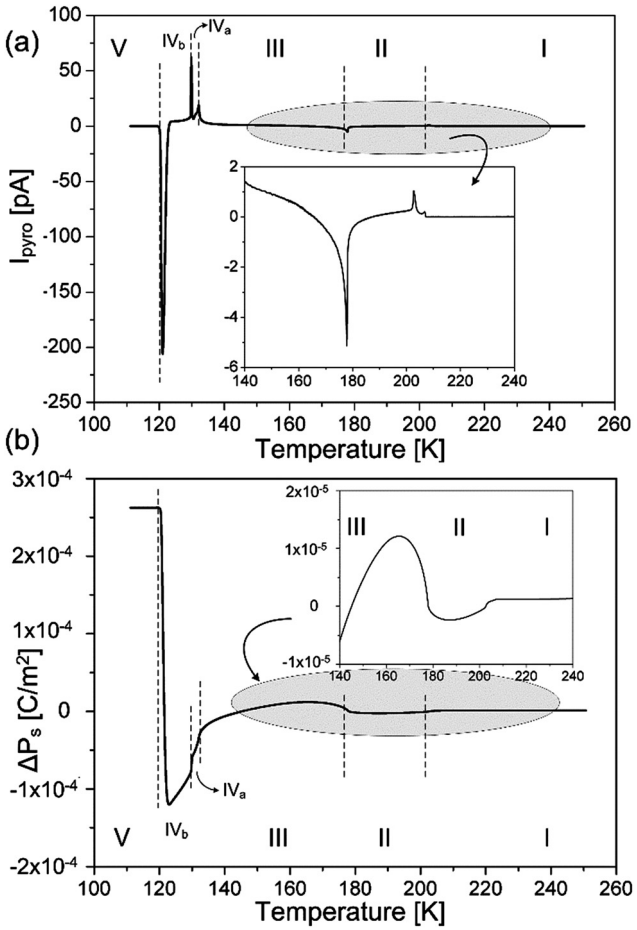

Fig. 9 Temperature dependence of (a) pyroelectric current and (b) corresponding spontaneous polarization changes for $FA_3Bi_2I_9$. Insets: Temperature dependence of ΔP_s in the vicinity of the I → II and II → III PTs.

100 K and then the measurements were carried out during heating. The results are shown in Fig. 9.

The peaks of I_{pyr} were observed for all the four PTs determined by the DSC method. In order to check if the values of the spontaneous polarization in the particular phases are reversible, we devised another measurement modality. This experiment was realized using four cycles, which are described below. The sample was pooled with the dc electric field of ±3 kV cm^{-1} across the I → II and II → III PTs and then the sample was short-circuited for 30 min in Phase III to eliminate the current due to the space charge. Then, the measurements were performed during heating up (2 K min^{-1}) to RT. The pyroelectric current shows two peaks at *ca.* 203 and 175 K first for the positive value of $+I_{pyro}$ and then for the negative one ($-I_{pyro}$), both of which were reversible in the positive/negative dc external field.

The resulting spontaneous polarization (ΔP_s) *versus* temperature (T) curves for these two cycles are shown in Fig. 10 (right side). The 3rd and 4th cooling cycles start (after pooling from RT) from 140 K (Phase III) down to 100 K. Two peaks appeared at 131 and 116 K and, similarly to the 1st and 2nd cycle, they exhibited an opposite polarity. The peaks of I_{pyr} were also reversible in the positive and negative dc external fields.

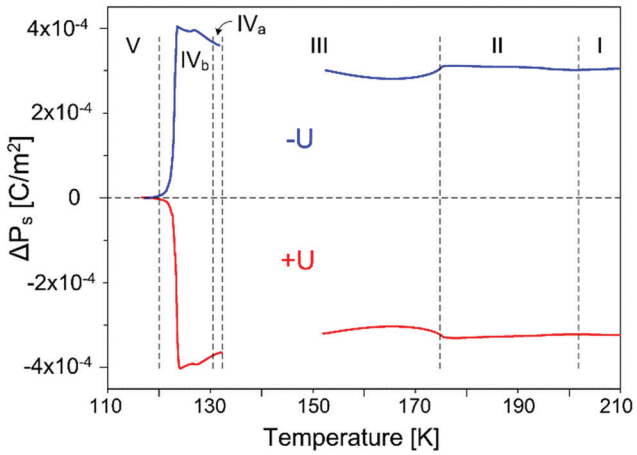

Fig. 10 Temperature changes of the spontaneous polarization, ΔP_s, of $FA_3Bi_2I_9$ after pooling by an external electric field.

The corresponding ΔP_s *versus* T curve is shown in Fig. 10 (left-hand side). Such a behavior of ΔP_s with temperature is extremely rare because in the temperature range described above, the pyroelectric coefficient (dP_s/dT) changes its sign three times. The most significant changes in ΔP_s, of the order of $\pm 4 \times 10^{-4}$ C m^{-2}, are visible near $T_{c(IV \rightarrow V)}$.

Observation of the hysteresis loop

The hysteresis loops measured at different temperatures (on cooling) are shown in Fig. 11. The presence of the reversible spontaneous polarization (P_s) is confirmed for all the low-temperature phases. It should be emphasized that the value of P_s (2×10^{-2} μC cm^{-2}) at 230 K is continuously reduced on cooling. To some extent, the behavior of P_s is in agreement with the pyroelectric measurements. Nevertheless, the real values of P_s in the subsequent phases are difficult to estimate because of two reasons: (i) a significant increase can be expected in the coercive field with

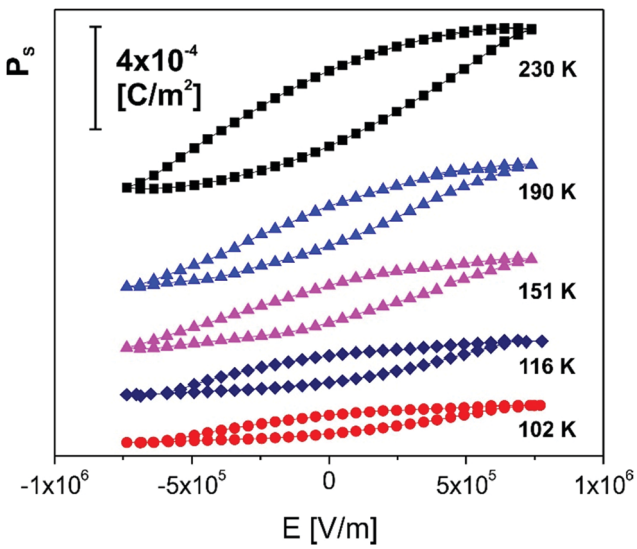

Fig. 11 *P*–*E* hysteresis loops at 230 K (Phase I), 190 K (Phase II), 151 K (Phase III), 116 K (Phase IV), and 102 K (Phase V).

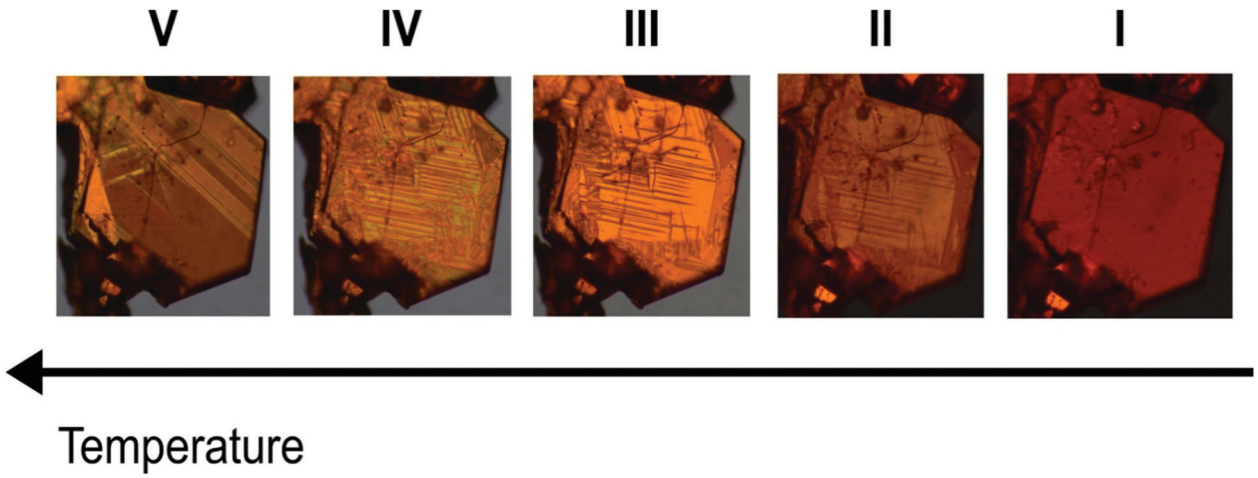

Fig. 12 Evolution of the ferroelastic domain pattern for $FA_3Bi_2I_9$ during the cooling cycle.

decreasing temperature, which does not enable us to obtain the saturated values of P_s and (ii) the possible change in the direction of the polar axis during the subsequent PTs.

Optical observations in polarized light

The results of the optical observations are shown in Fig. 12. In Phase I, the crystal shape corresponds to at least a 3-fold axis. The visible faces perpendicular to the plates form angles of 120°. The bulk of the crystal exhibits homogeneous transparency without ferroelastic domains.

The I → II PT proceeds very slowly and progressively. The contrast evolves from very faint to more intense. The transition may, therefore, be close to continuous. This is corroborated by a weak dielectric anomaly, which does not resemble a lambda anomaly, because the PT is between two polar phases. The domain pattern in Phase II results from the ferroelasticity implied by the point symmetry reduction $6mm \rightarrow 2mm$. The twin-law matrix of Table 1 corresponds to a mirror plane lost in the transition. In addition, a vanishingly small orthorhombic distortion of Phase II with respect to the hexagonal one is reflected in the angles between the visible domain walls, *e.g.*, $59.46^\circ \approx 60^\circ$. However, a shear deformation is also present because the inclusions of the domains within a region of different domains have typical lens-like shapes.[40] One of the domains yields a yellowish color and the two other ones are darker. A precise measurement of the angles and the shapes of the lenses may facilitate the structural resolution of the XRD experiment. The domain pattern becomes sharper after the II → III PT. This may result from an increase in the shear deformation, which is reflected in the angle, namely, 58.78°, which is more distant from 60°. The deformation is,

Table 1 Experimental details for $FA_3Bi_2I_9$

	Phase I	Phase II
Crystal data		
Crystal system, space group	Hexagonal, $P6_3mc$	Orthorhombic, $Cmc2_1$
Temperature (K)	220	190
a, b, c (Å)	8.711(2), 8.711(2), 22.014(9)	8.692(2), 15.055(2), 21.967(6)
V (Å^3)	1446.96(9)	2874.62(11)
Z	2	4
μ (mm^{-1})	21.75	21.89
Crystal size (mm)	0.15 × 0.11 × 0.10	0.15 × 0.11 × 0.10
Data collection		
T_{min}, T_{max}	0.625, 1.000	0.420, 1.000
No. of measured, independent and observed $[I > 2\sigma(I)]$ reflections	10 697, 1114, 995	12 711, 3803, 3157
R_{int}	0.040	0.036
$(\sin\theta/\lambda)_{max}$ (Å^{-1})	0.609	0.689
Refinement		
$R[F^2 > 2\sigma(F^2)]$, w$R(F^2)$, S	0.034, 0.088, 1.26	0.063, 0.206, 1.21
No. of reflections	1114	3803
No. of parameters	43	84
No. of restraints	8	12
H-Atom treatment	H-Atom parameters not refined	H-Atom parameters constrained
ρ_{max}, ρ_{min} (e Å^{-3})	0.91, −0.55	2.19, −2.72
Absolute structure	Refined as an inversion twin	Refined as merohedral twin, with twin matrix [−0.5 0.5 0 1.5 0.5 0 0 0 −1]
Absolute structure parameter	0.50(4)	

however, still too weak to allow the space group to be refined. The crystallographic system seems to remain orthorhombic. The satellites evident in Fig. 3 suggest the doubling of the unit cell. This may result in the presence of antiphase domain walls that are, however, not visible in the polarization microscopy images. In Phase IV, the domain pattern remains generally similar, but more inclusions occur. This may be related with the increasing shear deformation and compensation needed to preserve the integrity of the sample. Phase V exhibits a radical change in the domain pattern. The ferroelastic nature of the domains is, however, clear because the domain walls are neatly planar. The angles close to 60° suggest a hexagonal paraelastic phase.

An insight into the spatial orientation of the domain boundaries shows that the mirror and glide planes of the $P6_3mc$ group preserved in Phases II–IV are those marked in red in Fig. S4b (ESI†). Further, the shear planes corresponding to the domain boundaries are those marked in blue in this figure. In Phase V, in turn, the role of the planes seems to have interchanged because the angle between the prevailing domain boundaries in Phases IV and V are close to 30°. This would suggest an orthorhombic structure of Phase V stemming from $P6_3mc$, but with elementary cell edges along the blue lines in Fig. S4b (ESI†). The shear planes are those marked in red. The mutual orientation of the domain walls in Phases IV and V are shown in Fig. S5 (ESI†).

UV-vis light absorption

In the absorption spectrum (Fig. 13a), which extends from about 650 nm toward the UV region, one evident band can be distinguished with the maximum at about 510 nm (2.43 eV). Moreover, in the range of 475–350 nm, two less pronounced bands, at 420 nm (2.95 eV) and 365 nm (3.40 eV), are evident. The presence of these bands in the absorption spectrum is in agreement with the energy gaps between the valence band and band groups placed over the Fermi level found in the theoretical band structure (see Fig. 14).

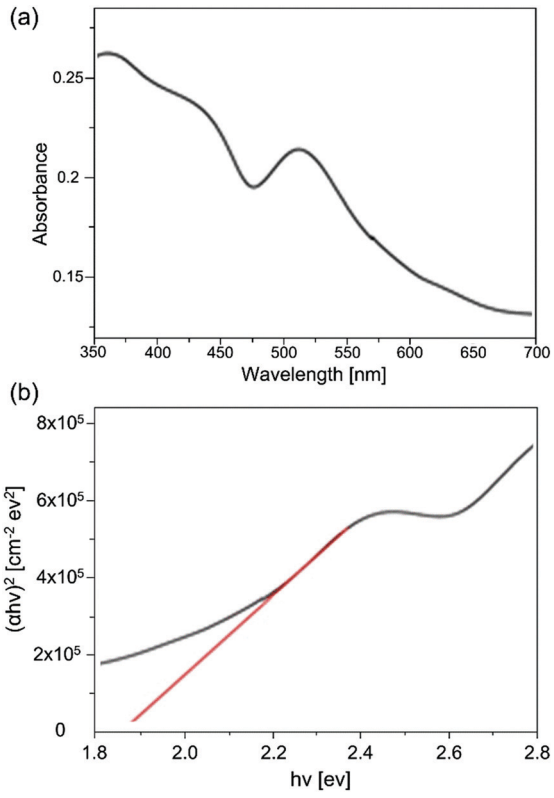

Fig. 13 (a) Absorption spectrum of $FA_3Bi_2I_9$; (b) Tauc plot for FBI, r = 1/2.

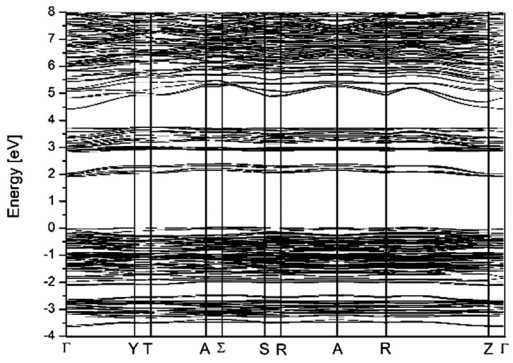

Fig. 14 Band structure of $FA_3Bi_2I_9$ with SOC taken into account. Analogous plot without SOC is shown in Fig. S6 (ESI†).

The bandgap, calculated using DFT taking the spin–orbit coupling (SOC) into account, is equal to 1.89 eV (Fig. 14), which effectively complies with the one determined using the Tauc plot, *i.e.*, 1.85 eV (Fig. 13b). When the SOC is neglected (Fig. S6, ESI†), the bandgap is about 0.5 eV higher than the former one, which indicates that the SOC is strong in the case of such systems. Based on the DFT calculations it is difficult to unequivocally state if the transition is of the direct or the indirect characteristic as the energy difference between these two transition types is lower than 0.1 eV. However, very good agreement between the calculated and experimentally determined bandgaps was achieved only when r = 1/2, which might indicate that the transition is of the direct allowed type.

The optical bandgap has been determined by a variant of the Tauc equation:

$$(\alpha h\nu)^{1/r} = A(h\nu - E_g) \quad (2)$$

where h is the Planck's constant, ν is the photon frequency, α is the absorption coefficient, E_g is the bandgap energy, and A is a proportionality constant.[41] The value of the $1/r$ exponent defines the nature of the electronic transitions, whether they are allowed or forbidden and whether they are direct or indirect.[42] Typically, allowed transitions dominate in basic absorption processes, resulting in either r = 0.5 or r = 2 for direct and indirect transitions, respectively.

Fig. S6 (ESI†) shows the band structure of $FA_3Bi_2I_9$, calculated without SOC (ESI†).

The PDOS (Fig. 15) indicates that the valence band is mainly composed of iodine-p states, while the conduction band is formed by the bismuth-p states. According to this, the transitions observed in the absorption spectrum can be assigned to I–Bi ligand–metal charge transfer (LMCT), which is characteristic of such systems.[43–45]

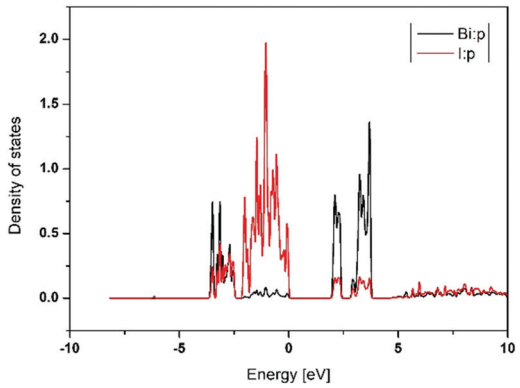

Fig. 15 PDOS of Bi-p and I-p states.

Discussion

It seems interesting to correlate the dielectric parameters of the discussed compound with the motif of the anionic networks and a type of organic cation placed in the cavities of the anionic substructure for $R_3M_2X_9$ stoichiometry. The data concerning these parameters are collated in Table 2.

Within the chemical stoichiometry $R_3M_2X_9$, the ferroelectricity is limited to two types of anionic sublayers among the four possible ones, namely, 0D discrete bi-octahedral units and 2D layers. A 2D structure is usually characteristic of chloride and bromide ferroelectrics containing only small alkylammonium or nonsubstituted ring (*e.g.*, pyrrolidine). For the 2D structure, organic cations (two types: R1 and R2), which occupy the cavities within the layers (R1), are highly disordered and are responsible for the ferroelectric order in the polar phases. Therefore, larger organic cations due to steric effects cannot occupy small vacancies in such layers. In turn, all the known iodide ferroelectrics possess a 0D anionic network and the restriction with respect to the size and symmetry of organic moieties are not apparent. The largest value of the electric permittivity close to T_c is observed for 2D ferroelectrics because easily polarizable anionic layers favor a long-range order of the dipole–dipole interactions. The influence of the dipole moment value, μ, is more obvious in the case of the spontaneous polarization values of ferroelectrics under consideration. Haloantimonate(III) and halobismuthate(III), characterized by 2D anionic structures, usually possess a smaller value of P_s in contrast to their 0D analogues, in spite of the fact that the organic cations of these crystals have larger μ values. Nevertheless, it should be noted that in the FA analogues, the cations possess a fairly small value of μ = 0.23 D, whereas those for the dielectric anomalies are fairly high (ε_{max} = 22). This suggests a significant contribution of the displacement, deformation, and polarization of ions. In summary, we can state that the relation between the structural parameters of crystals and their microscopic and macroscopic properties (P_s and ε_{max}) is more complicated and requires additional studies involving $R_3M_2X_9$-type compounds. The relationship between ferroelectricity and semiconducting properties (bandgap and usefulness in photovoltaics) is not clear even in well-known ABX_3 perovskites. It should be emphasized that in this work, we have studied the interplay between the ferroelectricity and semiconductor properties for the first time in this type of materials.

$FA_3Bi_2I_9$ is only the second example of $R_3M_2X_9$-type ferroelectric among haloantimonate(III) and halobismuthate(III) characterized by 0D anionic networks. FA cations possess the smallest dipole moment in the presented group of compounds; therefore, the ε_{max} value is fairly small. The ferroelectric properties of $FA_3Bi_2I_9$ are extended over all the phases, including the RT phase. $FA_3Bi_2I_9$ is extraordinarily thermally stable up to near 600 K, which is a very desirable feature for use in photovoltaic materials. The molecular mechanism of the detected PTs is complex, because it may be characterized by either "order–disorder" or "displacive" contributions. The continuous I → II and II → III PTs are due to the limitations in the reorientational motion of highly disordered FA cations and conjugated distortions of discrete $[Bi_2I_9^{3-}]$ units (see Fig. 16). The subsequent PTs, namely, II → III, III → IVa, IVb, and IV → V lead to the progressive freezing of the reorientational motion of cations. It seems, however, that the octahedral distortions, which are strongly related to the changes in the cationic positions, due to the presence of N–H···I and C–H···I HBs must also accompany successive structural transformations. The analysis of the crystal structure in Phases I and II reveals that the resulting nonzero spontaneous polarization in the *c*-direction comes from uncompensated dipoles of polar FA^+ cations.

Table 2 Ferroelectrics crystallizing with chemical stoichiometry $R_3M_2X_9$ (where M = Sb(III), Bi(III); R: organic cation). T_c: Curie Weiss temperature; 0D and 2D: zero- and two-dimensional anionic structures, P_s: spontaneous polarization; ε_{max}: maximum value at T_c or at ferroelectric–ferroelectric PT temperature; μ: dipole moment of the isolated molecule or cations in the crystal lattice (denoted as +)

Compound	T_c/K	Paraelectric phase	Ferroelectric phase	Anionic structure	$P_s \times 10^{-2}$ μC cm^{-2}	ε_{max}	μ/D
[Methylammonium]$_3Bi_2I_9$[46]	143	$P6_3/mmc$ $C2/c$	$P2_1$	0D	7.94–0.65	52	1.31 $(2.5–3.1)^+$
[Methylammonium]$_3Sb_2Br_9$[46,47]	134	$P\bar{3}m1$	—	2D	0.14–0.55	24	1.31
[Methylammonium]$_3Bi_2Br_9$[48,49]	101	$P\bar{3}m1$	Pm	2D	0.7	120	1.31
[Dimethylammonium]$_3Sb_2Br_9$[50]	164	$P2_1/c$	—	2D	0.8	120	1.03
[Dimethylammonium]$_3Sb_2Cl_9$[51]	242	$P2_1/a$	Pa	2D	0.69	1000	1.03
[Trimethylammonium]$_3Sb_2Cl_9$[52,53]	363	$P2_1/c$	Pc	2D	3.0	720	0.612
[*N*-Methylpyrrolidinium]$_3Sb_2Br_9$[12]	322	$R\bar{3}c$	$R3c$	0D	7.6	450	0.572
[*N*-Methylpyrrolidinium]$_3Sb_2Cl_9$[54]	323	$R\bar{3}c$	$R3c$	0D	5.2	250	0.572
[Pyrrolidinium]$_3Sb_2Cl_9$[55]	—	—	$R3m$-$P3$-$C2$	2D	0.004	115	1.58
[Formamidinium]$_3Bi_2I_9$[a]	—	—	6_3mc-$Cmc2_1$	0D	0.04	22	0.23^+

[a] This paper.

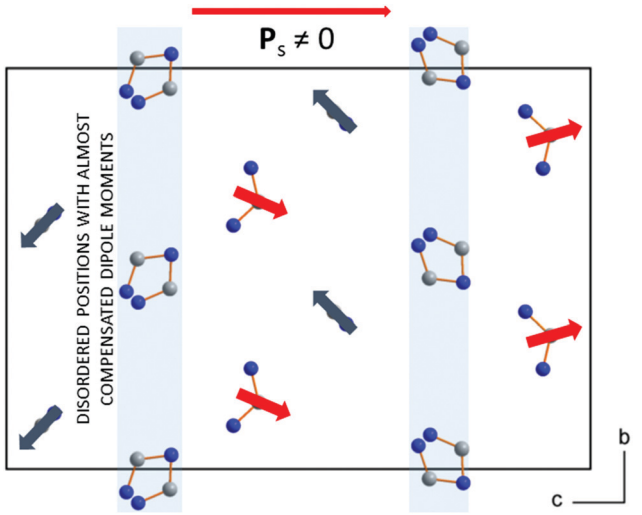

Fig. 16 Illustration of FA^+ dipoles (indicated by arrows) in partially ordered orthorhombic Phase II. Arrows are not drawn for disordered positions.

The presence of a distinct polar direction in FA^+ placements causes polar distortions of $[Bi_2I_9^{3-}]$ bi-octahedra.

$FA_3Bi_2I_9$ crystals are stable in a wide range of temperatures in the ambient atmosphere for months. Moreover, they exhibit worthwhile light-absorbing and semiconducting properties.

Conclusions

In summary, we have designed and synthesized a novel molecular-ionic ferroelectric within the haloantimonate(III) and halobismuthate(III) family based on the FA cation $[NH_2CHNH_2]_3$-Bi_2I_9. It crystallizes in the structure characterized by the discrete anionic form (face-shared bi-octahedra). This material undergoes a very complex sequence of five PTs, and the consequent low-temperature phases exhibit both ferroelectric and ferroelastic properties. Temperature-dependent single-crystal XRD, thermal methods, and dielectric spectroscopy measurements proved that the structural instability of the material is due to the changes in the dynamics of the FA cations and distortions of the anionic framework, which are both strongly coupled *via* HB interactions. The observed optical properties confirmed that the compound is a semiconductor with an optical bandgap value of 1.85 eV, whereas that calculated using DFT, taking SOC into account, is 1.89 eV. The bandgap energy determined from σ_{AC} is equal to $\sim$0.7 eV, which is smaller than that estimated from the UV-vis spectra. Such smaller values are usually observed for these types of compounds. This observation requires further investigations. The intriguing dielectric properties, including RT ferroelectricity, relatively small bandgap, very good moisture stability, and lead-free composition, make $[NH_2CHNH_2]_3Bi_2I_9$ a serious candidate for optoelectronic applications.

Conflicts of interest

There are no conflicts to declare.

Acknowledgements

DFT calculations have been performed using resources provided by Wroclaw Centre for Networking and Supercomputing (http://wcss.pl), grant no. 415. This work has been supported by the Polish Ministry of Science and Higher Education Agreement No. 3807/ZIBJ DUBNA/2017/0 and partially by the International Program Joint Institute for Nuclear Research Dubna no. 04-4-1121-2017/2020.

Notes and references

1 M. Saliba, T. Matsui, J.-Y. Seo, K. Domanski, J.-P. Correa-Baena, M. K. Nazeeruddin, S. M. Zakeeruddin, W. Tress, A. Abate, A. Hagfeldt and M. Grätzel, *Energy Environ. Sci.*, 2016, **9**, 1989.
2 M. Saliba, T. Matsui, K. Domanski, J.-Y. Seo, A. Ummadisingu, S. M. Zakeeruddin, J.-P. Correa-Baena, W. R. Tress, A. Abate, A. Hagfeldt and M. Grätzel, *Science*, 2016, **354**, 206.
3 A. Stroppa, D. Di Sante, P. Barone, M. Bokdam, G. Kresse, C. Franchini, M. Whangbo and S. Picozzi, *Nat. Commun.*, 2014, **5**, 5900.
4 O. Weber, D. Ghosh, S. Gaines, P. F. Henry, A. B. Walker, M. S. Islam and M. T. Weller, *Chem. Mater.*, 2018, **30**, 3768.
5 M. Owczarek, R. Jakubas, A. Pietraszko, W. Medycki and J. Baran, *Dalton Trans.*, 2013, **42**, 15069.
6 S. A. Adonin, M. N. Sokolov and V. P. Fedin, *Coord. Chem. Rev.*, 2016, **312**, 1.
7 N. Leblanc, N. Mercier, L. Zorina, S. Simonov, P. Auban-Senzier and C. Pasquier, *J. Am. Chem. Soc.*, 2011, **133**, 14924.
8 W. H. Bi, N. Leblanc, N. Mercier, P. Auban-Senzier and C. Pasquier, *Chem. Mater.*, 2009, **21**, 4099.
9 N. Mercier, *Eur. J. Inorg. Chem.*, 2013, 19.
10 R. Jakubas, G. Bator and Z. Ciunik, *Phys. Rev. B: Condens. Matter Mater. Phys.*, 2003, **67**, 1.
11 A. Miniewicz, J. Sworakowski, R. Jakubas, M. Bertault and C. Ecolivet, *Ferroelectrics*, 1989, **94**, 323.
12 Z. Sun, A. Zeb, S. Liu, C. Ji, T. Khan, L. Li, M. Hong and L. Luo, *Angew. Chem., Int. Ed.*, 2016, **55**, 11854.
13 A. Piecha, A. Białonska and R. Jakubas, *J. Mater. Chem.*, 2012, **22**, 333.
14 W.-P. Zhao, C. Shi, A. Stroppa, D. Di Sante, F. Cimpoesu and W. Zhang, *Inorg. Chem.*, 2016, **55**, 10337.
15 A. Piecha, A. Pietraszko, G. Bator and R. Jakubas, *J. Solid State Chem.*, 2008, **118**, 1155.
16 N. A. Yelovik, A. V. Mironov, M. A. Bykov, A. N. Kuznetsov, A. V. Grigorieva, Z. Wei, E. V. Dikarev and A. V. Shevelkov, *Inorg. Chem.*, 2016, **55**, 4132.
17 D. Frejd, C. B. Hassena, S. Elleuchb, H. Fekib, N. C. Boudjadac, T. Mhiria and M. Boujelbenea, *Mater. Res. Bull.*, 2017, **85**, 23.
18 A. Piecha, R. Jakubas, A. Pietraszko and J. Baran, *J. Mol. Struct.*, 2007, **844–845**, 132.
19 D. Ran, L. He, Z. Xiaoli, X. Juanxiu, K. Rahul, S. Huaxi, Z. Bowen, C. Geng, G. Fei, F. Xiaohua, C. Jingsheng,

C. Xiaodong, S. Xiaowei and Z. Yuanjin, *Adv. Funct. Mater.*, 2016, **26**, 7708.
20 M. Rok, A. Piecha-Bisiorek, P. Szklarz, G. Bator and L. Sobczyk, *Chem. Phys.*, 2015, **452**, 53.
21 P. Blaha, K. Schwarz, P. Sorantin and S. B. Trickey, *Comput. Phys. Commun.*, 1990, **59**, 399.
22 J. P. Perdew, K. Burke and M. Ernzerhof, *Phys. Rev. Lett.*, 1996, **77**, 3865.
23 A. Kokalj, *Proc. Symp. Softw. Dev. Process Mater. Des.*, 2003, **28**, 155.
24 R. Jakubas and L. Sobczyk, *Phase Transitions*, 1990, **20**, 163.
25 P. Szklarz, A. Pietraszko, R. Jakubas, G. Bator, P. Zieliński and M. Gałązka, *J. Phys.: Condens. Matter*, 2008, **20**, 1.
26 M. Węcławik, A. Gągor, R. Jakubas, A. Piecha-Bisiorek, W. Medycki, J. Baran, P. Zielinski and M. Galazka, *Inorg. Chem. Front.*, 2016, **3**, 1306.
27 O. Lindqvist, *Acta Chem. Scand.*, 1968, **22**, 2943.
28 G. J. Wessel and D. J. W. Ijoo, *Acta Crystallogr.*, 1957, **10**, 466.
29 B. Chabot and E. Parthe, *Acta Crystallogr., Sect. B: Struct. Crystallogr. Cryst. Chem.*, 1978, **34**, 645.
30 M. Guymont, *Phys. Rev. B: Condens. Matter Mater. Phys.*, 1978, **18**, 5385.
31 K. Aizu, *Phys. Rev. B: Condens. Matter Mater. Phys.*, 1970, **2**, 754.
32 G. A. Jeffrey, *An Introduction to Hydrogen Bonding*, Oxford University Press, Oxford, 1997.
33 A. Gągor, G. Banach, M. Węcławik, A. Piecha-Bisiorek and R. Jakubas, *Dalton Trans.*, 2017, **46**, 16605.
34 A. Gągor, M. Węcławik, B. Bondzior and R. Jakubas, *CrystEngComm*, 2015, **17**, 3286.
35 D. H. Fabini, G. Laurita, J. S. Bechtel, C. C. Stoumpos, H. A. Evans, A. G. Kontos, Y. S. Raptis and P. Falaras, *J. Am. Chem. Soc.*, 2016, **138**, 11820.
36 E. C. Schueller, G. Laurita, D. H. Fabini, C. C. Stoumpos, M. G. Kanatzidis and R. Seshadri, *Inorg. Chem.*, 2018, **57**, 695–701.
37 M. E. Fleet, *Mineral. Mag.*, 1976, **40**, 531.
38 J. M. Perez-Mato, D. Orobengoa and M. I. Aroyo, *Acta Crystallogr., Sect. A: Found. Crystallogr.*, 2010, **66**, 558.
39 A. K. Jonscher, *Nature*, 1977, **267**, 673.
40 A. Tagantsev, L. E. Cross and J. Fousek, *Domains in Ferroic Crystals and Thin Films*, Springer, New York, 2010, p. 239.
41 E. A. Davis and N. F. Mott, *Philos. Mag.*, 1970, **22**, 903.
42 B. D. Viezbicke, S. Patel, B. E. Davis and D. P. Birnie, *Phys. Status Solidi B*, 2015, **252**, 1700.
43 A. J. Lehner, D. H. Fabini, H. A. Evans, C.-A. Hébert, S. R. Smock, J. Hu, H. Wang, J. W. Zwanziger, M. L. Chabinyc and R. Seshadri, *Chem. Mater.*, 2015, **27**, 7137.
44 M. Lyu, J.-H. Yun, M. Cai, Y. Jiao, P. V. Bernhardt, M. Zhang, Q. Wang, A. Du, H. Wang, G. Liu and L. Wang, *Nano Res.*, 2016, **9**, 692.
45 N. A. Yelovik, A. V. Mironov, M. A. Bykov, A. N. Kuznetsov, A. V. Grigorieva, Z. Wei, E. V. Dikarev and A. V. Shevelkov, *Inorg. Chem.*, 2016, **55**, 4132.
46 R. Jakubas, J. Zaleski and L. Sobczyk, *Ferroelectrics*, 1990, **108**, 105.
47 J. Mróz and R. Jakubas, *Ferroelectr., Lett. Sect.*, 1994, **17**, 73.
48 R. Jakubas, J. Lefebvre, H. Fontaine and P. Francois, *Solid State Commun.*, 1992, **81**, 139.
49 R. Jakubas, U. Krzewska, G. Bator and L. Sobczyk, *Ferroelectrics*, 1988, **77**, 129.
50 J. Zaleski, C. Pawlaczyk, R. Jakubas and H.-G. Unruh, *J. Phys.: Condens. Matter*, 2000, **12**, 7509.
51 R. Jakubas, *Solid State Commun.*, 1986, **60**, 389.
52 A. Kallel and J. W. Bats, *Acta Crystallogr., Sect. C: Cryst. Struct. Commun.*, 1985, **41**, 1022.
53 R. Jakubas, Z. Czapla, Z. Galewski and L. Sobczyk, *Ferroelectr., Lett. Sect.*, 1985, **5**, 143.
54 C. Ji, Z. Sun., A. Zeb, S. Liu, J. Zhang, M. Hong and J. Luo, *J. Phys. Chem. Lett.*, 2017, **8**, 2012.
55 M. Wojciechowska, A. Gągor, A. Piecha-Bisiorek, R. Jakubas, A. Ciżman, J. Zaręba, M. Nyk, P. Zieliński, W. Medycki and A. Bil, *Chem. Mater.*, 2018, **30**, 4597.

